Effect of the Co_3O_4 load on the performance of $PdO/Co_3O_4/ZrO_2$ open cell foam catalysts for the lean combustion of methane: kinetic and mass transfer regimes

Carmen W. Moncada Quintero, Giuliana Ercolino, Stefania Specchia**

Politecnico di Torino, Department of Applied Science and Technology, Corso Duca degli Abruzzi 24, 10129 Torino, Italy

* Corresponding authors: carmen.moncada@polito.it, stefania.specchia@polito.it

Highlights

- Pore and strut diameter distribution of zirconia open cell foam.
- Effect of Co_3O_4 amount on the catalytic performance for the complete CH_4 oxidation.
- Pd-PdO transformation by varying the carrier amount and inlet CH_4 concentration.
- Evaluation of kinetic, intraparticle and interphase mass transfer resistances.
- Mass transfer correlation for ceramic open cell foam a low *Re* numbers.

Abstract

In this study, kinetic and mass transfer resistances (pore and interphase diffusion) were evaluated by varying the Co_3O_4 amount in the catalyst (PdO/Co_3O_4) supported on the zirconia open cell foam (Zir-OCF) of 30 ppi. The catalytic performance was examined toward the methane combustion in lean conditions (0.5 and 1.0 vol.% CH_4 inlet concentration, O_2/CH_4 molar ratio 8, WHSV 30, 60 and 90 NL h^{-1} g_{cat}^{-1}). Pore and strut geometry of the bare foam were evaluated by SEM images and X-CT data analysis. Solution combustion synthesis was employed to line the Co_3O_4 spinel on the foam, while the wetness impregnation for the PdO on the spinel. The various resistances were evaluated and compared at different WHSV by varying the Co_3O_4 amount. Finally, we derived a correlation that describes the mass transfer in OCFs at low Reynolds numbers.

Graphical Abstract

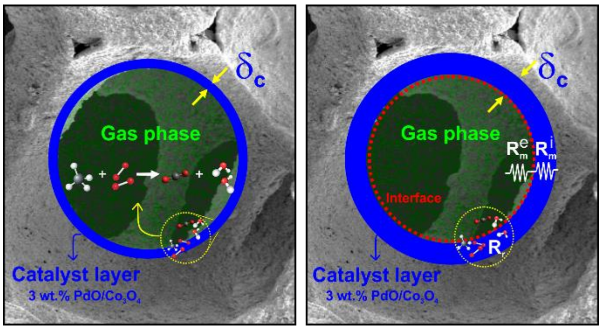

Keywords

Controlling resistances; catalyst loading; catalyst thickness; mass transfer; Pd-PdO transformation; methane combustion.

Article Info

The Authors dedicate this paper to Professors José Antonio Odriozola (University of Sevilla, Spain) and Mario Montes (University of the Basque Country, Spain), on the occasion of their 65th birthday.

1. Introduction

Open cell foams (OCFs) have become an excellent candidate for a multiplicity of industrial applications, thanks to the combination of their attractive features such as high porosity, large specific surface area and mechanical strength as well as high fluid flow permeability and lightness [1–3]. In chemical engineering, OCFs are used as attractive catalytic supports since they offer a lower pressure drop compared to conventional fixed bed reactors [4–8]. In addition, their particular structural geometry produces a tortuous flow path that improves mixing and thus mass transfer compared to other catalytic supports such as monolith and honeycombs, resulting in high catalyst activity per unit volume [7,9–14]. In recent years, several research groups have made efforts to study and quantify mass transfer in OCFs both experimentally and computational simulations [4,15–21]. Richardson et al. [15] studied the mass transfer during the CO oxidation on Pt/γ-Al_2O_3-coated alumina ceramic foam of 30 ppi. They demonstrated that the flow through the foam follows exactly the same convective fluid mechanics principles as in packed beds of equivalent diameter (volume/surface ratio). Later, Giani et al. [4]

measured the mass transfer coefficients for the CO combustion over Pd/γ-Al_2O_3 washcoated metallic foams with different nominal cell size. The authors found that the mass transfer values obtained during their experiments resembled those estimated from semi-theoretical literature correlations for heat transfer in flow across series of tubes at low Reynolds numbers. They further expanded their work by deriving a generalized correlation valid for both ceramic and metallic foams [17]. On the other hand, Incera Garrido et al. [5] estimated the mass transfer coefficients over Pt/SnO_2-coated ceramic foams by monitoring the CO oxidation for foams with porosities between 75% and 85%, and pore counts between 10-45 ppi. A geometric factor was implemented to obtain a single descriptor in terms of pore density and void fraction.

Recently, Aguirre et al. [21] analyzed the mass transfer with a series of experiments and numerical simulations using the oxidation of CO on Pt/γ-Al_2O_3/metallic foam as reaction model. They derived a correlation with an asymptotic value of Sherwood number of 1.94, assuming the foam with a structure described by the Kelvin cell model. This correlation obtained a slightly higher dependence between the Sherwood number and Reynolds numbers when compared to the above mentioned studies. However, most of these correlations have been derived for Reynolds much larger than 10, making them inaccurate for the description of catalytic processes at low flow rates. Besides, most of these studies were focused only on the external mass transfer effects, ignoring the relative importance of pore diffusion effects (inside the catalyst layer). In fact, in such studies it was assumed that conversion in foam-based reactors changes from kinetically limited to external mass transfer limited directly, without taking into account the effect of the catalyst thickness and its influence on the measurement of the mass transfer coefficients. Von Rickenbach et al. [22] demonstrated that the diffusion within the catalyst layer in OCFs is considerable even at high values of mass transfer coefficient. Thus, a careful evaluation of each controlling regime (kinetic, internal, and external diffusion) should be checked to effectively determine external mass transfer coefficients.

In our previous work, the catalytic performance of 3 wt.% PdO/Co_3O_4 catalyst in lean conditions was studied, either in powder [23] or structured form [7,24,25], at different weight hourly space velocity (WHSV, 30,60,90 NL h^{-1} g_{cat}^{-1}) and inlet methane concentrations (0.5-1%). In those studies, the structured catalysts were prepared by covering the OCFs with the same amount of catalyst (~200 mg), such that the catalytic thickness was kept roughly constant. In addition, we carefully analyzed the heat and mass transfer during the complete methane combustion in lean conditions on three different ceramic OCF materials (zirconia, silicon carbide, and alumina) [25]. We obtained that the best catalytic performance in terms of CH_4 conversion, heat transfer, and mass was obtained for the Zirconia-OCF (Zir-OCF) one. In this work, we focused our attention on studying the different control resistances (kinetic, pore, and interphase diffusion) and the effect on the catalytic performance by increasing the Co_3O_4 amount in the catalyst (3 wt.% PdO/Co_3O_4) coated on the 30 ppi Zir-OCF by performing the CH_4 oxidation in lean conditions. First of all, we characterized the pore and strut geometry of the bare foams by a series of accurate SEM and X-CT analyses. Then, the Co_3O_4 spinel was deposited on the foams by solution combustion synthesis, while the PdO via wetness impregnation. The catalyst tests were performed at different WHSV and concentrations of methane (0.5 and 1 vol.%). The various resistances were evaluated and compared at different WHSV by varying the Co_3O_4 amount. Finally, we derived a correlation that describes the mass transfer in OCFs at low Reynolds numbers.

2. Materials and methods

2.1. Open cell foams and Chemicals

Cobalt (II) nitrate hexahydrate $Co(NO_3)_2{\cdot}6H_2O$ (purity ≥ 98%), palladium(II) nitrate hydrate $Pd(NO_3)_2{\cdot}xH_2O$ (≥99% purity), glycine NH_2CH_2COOH (purity ≥ 99%), isopropyl alcohol $CH_3CHOHCH_3$ (purity ≥99.7%), and ethanol CH_3CH_2OH (purity ≥99.8%) were purchased from Sigma-Aldrich. Ultrapure water (Millipore Milli-Q system with a resistivity ≈ 18 MΩ cm) was used to prepare the aqueous solutions. Methane, oxygen, and nitrogen gases (purity 99.999%) flowed from cylinders purchased from SIAD Company. Zirconia open cell foams (Zir-OCFs) with pore density of 30 ppi (Vukopor® HT30) were purchased from Lanik S.r.o. (Czech Republic). The overall dimensions of Zir-OCFs were of 30 mm as length and 9 mm as diameter.

2.2. Preparation of the structured catalysts

Firstly, the Zir-OCFs were washed for 30 min in a solution of water/acetone (50/50 vol.%) using an ultrasonic bath at room temperature and dried for 60 min at 140 °C. The cleaned OCFs were used as support for three different amounts of Co_3O_4 catalyst (100, 150, and 250 mg, respectively), which were deposited on Zir-OCFs via SCS, as described in detailed in our previous works [7,25–27]. Briefly, the Zir-OCFs were dipped for 3 minutes in a 3 M cobalt nitrate and glycine solution (amount of glycine equal to 0.25 compared to the stoichiometric amount). The excess of the solution was removed with compressed air. The wet OCFs were placed in a furnace at 250 °C for 20 min to allow the ignition of the combustion reaction. The coating process was repeated several times until the desired amount of Co_3O_4 carrier was achieved. Finally, the Co_3O_4-coated Zir-OCFs were calcined at 600 °C for 4 h in static air. Then, 3 wt.% PdO was deposited on the Co_3O_4-coated Zir-OCFs by incipient wetness impregnation using an aqueous solution of palladium nitrate. After each dipping, the wet OCFs were dried at 140 °C for 1 h and then calcined at 600 °C for 4 h in static air. **Table 1** shows the overall catalyst loading for the three Co_3O_4 amounts employed. Such values account also for the PdO present on each OCF prepared. **Table S1** in the *Supplementary Data* lists the exact amounts of Co_3O_4 and PdO loaded on the three OCFs prepared ($W_{Co_3O_4}$and W_{PdO}).

As a quick test before testing the reactivity of the prepared OCFs, we tested the adhesive properties of the coated catalytic layers via sonication (S3M 2200 device by Sonica). Briefly, as also described in our previous works [7,11,12,25], we immersed the prepared OCFs in a solution of 50/50 water/isopropyl alcohol and sonicated for 2 h at 40 kHz and 130 W. The difference of weight before and after sonciation was taken as an indication of the adhesion of the catalty coating over the foams.

Table 1. Overall catalyst loading (3 wt.% PdO/Co_3O_4) for the three OCFs prepared by varying the Co_3O_4 amount: 100 (C_{load}^{100}), 150 (C_{load}^{150}) and 250 (C_{load}^{250}) mg on Zir-OCF.

Catalyst loading : mg_{cat} cm^{-2}_{OCF}		
C_{load}^{100}	C_{load}^{150}	C_{load}^{250}
6.1	8.2	13.7

2.3. Catalytic tests toward CH_4 combustion

The catalytic activity towards CH_4 oxidation of the three OCFs coated with the different amounts of Co_3O_4 (100, 150, and 250 mg) was tested in a lab-scale fixed-bed reactor (a straight quartz tube, 10 mm ID), inserted in a PID-regulated electrical oven. Each Zir-OCF, wrapped in a thin vermiculite foil to avoid channeling phenomena and heat dispersion, was placed at the center of the reactor and the oven was heated up to 700 °C flowing 0.1 NL min^{-1} of N_2 with a heating rate of 10 °C min^{-1}. Once the set temperature has been reached, the reactive $CH_4/O_2/N_2$ gas mixture was fed (various runs performed at 0.5 or 1.0 vol.% of CH_4, 4.0 or 8.0 vol.% of O_2 in N_2, keeping constant the O_2/CH_4 molar ratio to 8 to assure lean conditions). When the combustion reaction reached steady state conditions at 700 °C (complete conversion of CH_4), the reactor was cooled down up to room temperature with a cooling rate of 5 °C min^{-1}, while measuring the outlet dry gas concentrations as a function of the temperature. A K-type thermocouple located few mm inside the inlet side of the OCF monitored the reaction temperature. An ABB analyzer equipped with a NDIR module Uras 14 for $CO/CO_2/CH_4$ and a paramagnetic module Magnos 106 for O_2 (water vapor was removed before entering the analyzer in a condenser set at 3 °C) was used to analyze the reactor outlet dry gas composition. The reagents flow rate was varied between 50 to 400 NmL min^{-1}, to perform catalytic tests at three different values of the weight hourly space velocity (WHSV, 30, 60, and 90 NL h^{-1} g_{cat}^{-1}, respectively). Such WHSV has been maintained considering the amount of effective mass of catalyst, that is, $W_{cat} = W_{PdO} + W_{Co_3O_4}$ (**Table S1**). The reproducibility of the results was assure by repeating each catalytic run for at least three times.

2.4. Characterization of the pore and strut size

Scanning Electron Microscope (SEM) images were acquired by FESEM Leo 50/50 VP equipped with a Gemini-type column to evaluate the textural properties of the bare Zir-OCFs. SEM images were obtained from small pieces of the bare structure with an accelerating voltage of 8 kV and a working distance of 30 mm.

X-ray Computed Tomography (X-CT) was carried out with an Xradia MicroXCT 400 scanner in order to determine the geometric structural parameters of the foams. High resolution scans were employed with an objective lens of 1X and voxel size of 22 μm. The sample was placed on a rotating plate between the X-ray source and the detector. X-ray images were collected by rotating 360° each sample, with an angular rotation interval of 0.3 degrees and exposure time of 4 s, resulting in 1233 images per sample. The X-ray power was set to 8 Watts and 80 kV. The Xradia's filtered back-projection algorithm was used to reconstruct CT slices. The images were then processed using the freeware program FIJI ImageJ. A sub-volume of the CT scan was selected (630x630x550) to eliminate uninteresting areas from the processing analysis. Then, a Gaussian filter was used to blur and remove noise from images [28]. This filter allows to smooth the region of interests and reduce the smoothening in the vicinity of edges. Lastly, high-signal (void filled with fluid phase) and low-signal (solid ceramic material) regions can be identified by converting the gray-scale CT data into a binary format, with an iterative procedure based on the isodata algorithm to obtain the gray level threshold [29]. The threshold value was checked using the Otsu method on the same gray-scale CT data [30–33]. Single spots of noise remained were removed by tagging the groups of connected voxels, calculating their number of solid voxels and removing all groups below the thresold limit of ten solid voxels, according to Marseille method [28]. Finally, a morphological closing operation followed by filling of the hollow struts. **Figure 1** shows the different steps of image processing by using FIJI ImageJ.

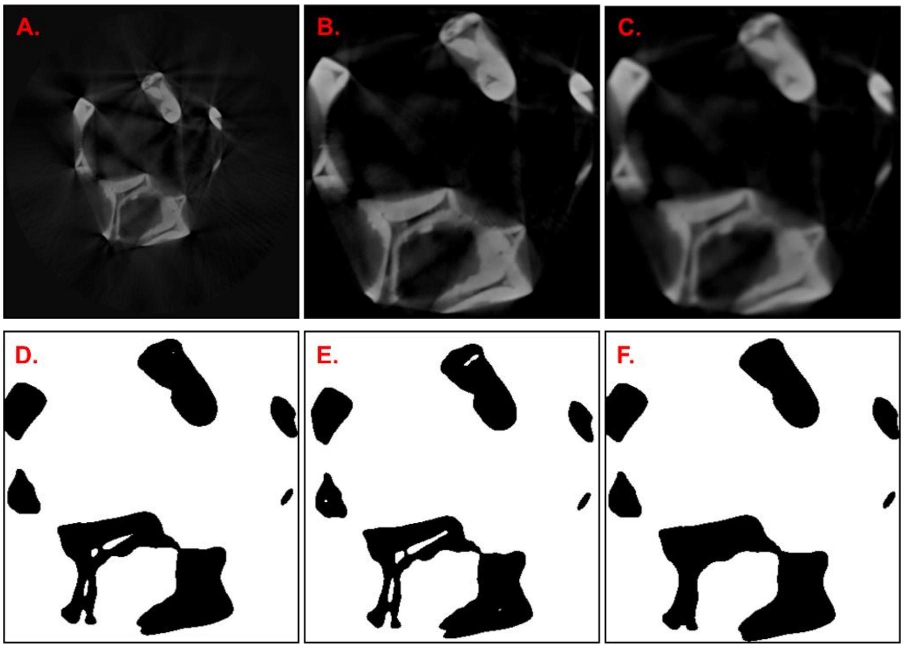

Figure 1. Image processing steps: **(A)** Original image, **(B)** Cut image, **(C)** Gaussian filtered image, **(D)** Setting binary format, **(E)** Threshold checked by Otsu method, **(F)** Noise elimination, closing morphological operation and filling of inner void struts. The images are slices of a 3D matrix.

An image analysis was carried out for the characterization of the pore and strut diameters using the same open software. First of all, we assume a circular shape of the foam pore, thus the area of each pore was accurately evaluated by the software and then the diameter of an equivalent circle was determined as shown in **Figure 2A**. As reported in our previous work [25], the circular pore shape assumption can be perfectly adopted for the analysis of OCFs as catalytic supports, even if some pores are oval. This assumption does not invalidate the results on heat and mass transfer, being the difference between assuming pores oral or circular extremely limited [25]. The strut thickness was measured in the middle of the strut length (**Fig. 2B**). More than 100 pore and strut measurements were analyzed and the average diameter was calculated as an arithmetic mean. Pore and strut size distributions were obtained from X-CT data and SEM images, where the mean pore and strut size of the sample was determined using the Gaussian peak fitting module of OriginPro 8 software.

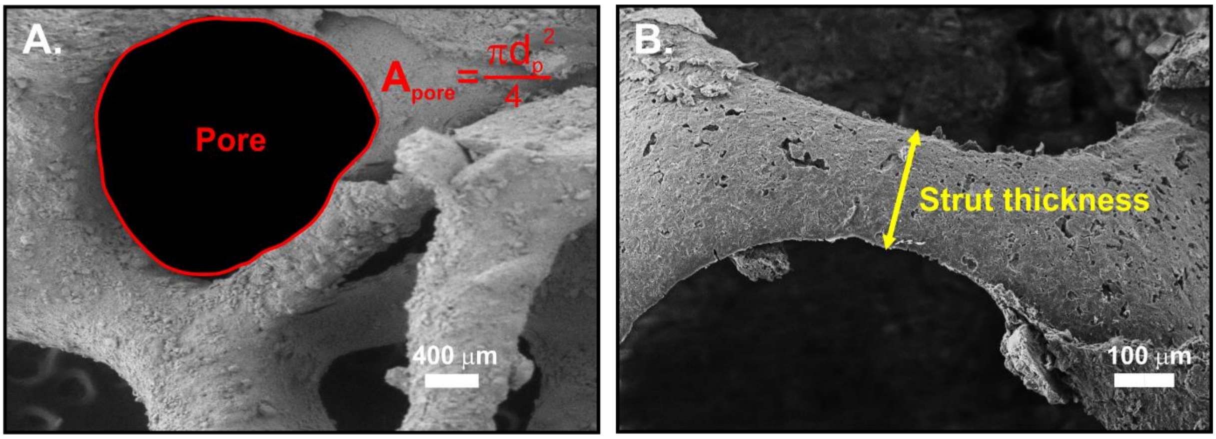

Figure 2. Image analysis: Pore **(A)** and strut **(B)** size evaluation.

2. Results and Discussion

2.1 Characterization of pore and strut diameter

Figure 3 shows a comparison of the strut diameter distribution obtained from the X-CT data and SEM images. As can be seen, the strut diameter distribution plots were deconvoluted into two peaks (using Gaussian distribution) corresponding to two different strut sizes along the strut length for both characterization techniques (**Fig. 3A** and **3B** from X-CT data and SEM images, respectively). The mean strut size of the first peak was taken as the characteristic thickness (corresponding to the thinnest part of the strut). The second peak showed practically the same mean strut value (approximately 0.50 mm) for both measurements, with a higher frequency for the X-CT measurements. On the other hand, the pore distribution plots showed a narrow Gaussian distribution with a slightly larger mean pore diameter for the data extracted from the X-CT than those obtained from the manual measurements of the SEM images (**Fig. 3C**/X-CT-data and **3D**/SEM images). **Table 2** shows a comparison of the nominal geometrical properties provided by the manufacturer and those obtained from the tomography data of the 30 ppi zirconia foam.

Table 2. Nominal and measured (by X-CT images) geometrical properties of the Zir-OCF with 30 ppi.

	d_s [mm]	d_p [mm]	ε_o	S_v [mm^{-1}]
Nominal	0.85	2.20	0.84	1.308
X-CT data	0.43	1.38	0.85	1.015

From **Table 2**, it can be seen that the nominal size of pore and strut are higher than those obtained from X-CT images. The difference between such values could be due to manufacturing defects or irregularities of the cellular structure, as well as a possible overestimation of the diameters by the manufacturer [5]. It is also important to mention that the open porosity was estimated by measuring the remaining void volume after the artificial filling of cavities within the solid phase. Because the resolution of the X-CT in this study was lower than the size of certain microscopic pores in the solid phase (strut), only the open porosity of zirconia foam was characterized.

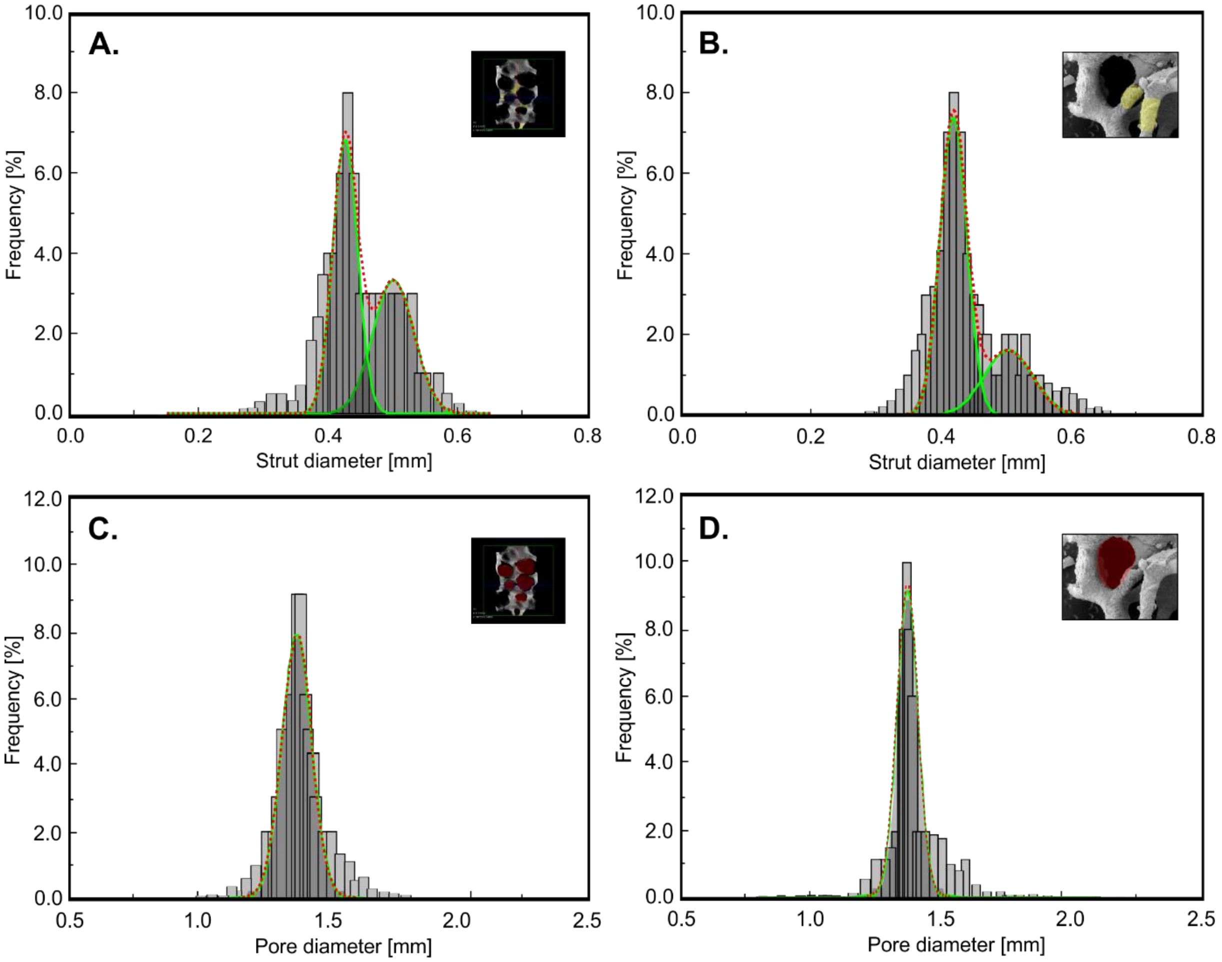

Figure 3. Strut and pore size distribution from X-CT data **(A/C)** and SEM images **(B/D).**

2.2 Catalytic tests toward CH_4 lean combustion

Ahead of the catalytic tests, we checked the adhesive properties of the catalysts' layers coated over the foams via sonication. The adherence values were 98.6 % for the C_{load}^{100}, 98.4% the C_{load}^{150} and 98.1% the C_{load}^{200}, respectively. A weight percentage loss of catalyst layer ranging between 1 and 2% after sonication is a sign of excellent adhesion of the catalyst on the ceramic foam, and perfectly in line with literature results [7,12,25,34]. Interestingly, an increase of the catalyst loading, corresponding to a thicker later of catalyst covering the surface of the foam, does not lead to a dramatic loose of the catalyst itself. This result is a clear sign of the compactness of the catalyst and its optimal adhesive properties.

Figure 4 shows the catalytic performance in lean methane combustion for the three PdO/Co_3O_4-coated Zir-OCF catalysts (with 3 wt.% of PdO on Co_3O_4 carrier) at different WHSV (30, 60, and 90 NL h^{-1} g_{cat}^{-1}) and inlet CH_4 concentrations. The curves reported in **Figure 4** are explicative of the best conversion profiles obtained during the cooling phase of the tests. In fact, conversion curves during the cooling phase are more favorable, considering the hysteresis due to either the existence of multiple steady-states [35–37] and the PdO-Pd transition [38–40], which decreases the rate of CH_4 combustion. **Figures S.1 and S.2** in the *Supplementary Data* shows all the tests performed, with repeatability and standard deviation on the T_{50}. As expected, the increase of WHSV leads to worsening of the combustion process, with a shift of CH_4 conversion curves toward higher temperatures, because of the reduction of contact time between the catalyst and reactants. In fact, at WHSV of 30, the complete conversion of CH_4 is achieved at temperatures between 380 and 630 °C depending on both the catalyst amount and the inlet CH_4 volume fraction, while at WHSV of 90, only the catalyst with a loading of 6.1 mg_{cat} $cm^{-2}{}_{OCF}$ (C_{load}^{100}) reached full conversion of CH_4 at temperatures below 700 °C for both the inlet CH_4 concentrations. Furthermore, when comparing the catalytic performance at 0.5 and 1 vol.% CH_4 as inlet concentration, a slight improvement in terms of conversion is observed at lower concentrations for all WHSV and catalyst loading investigated.

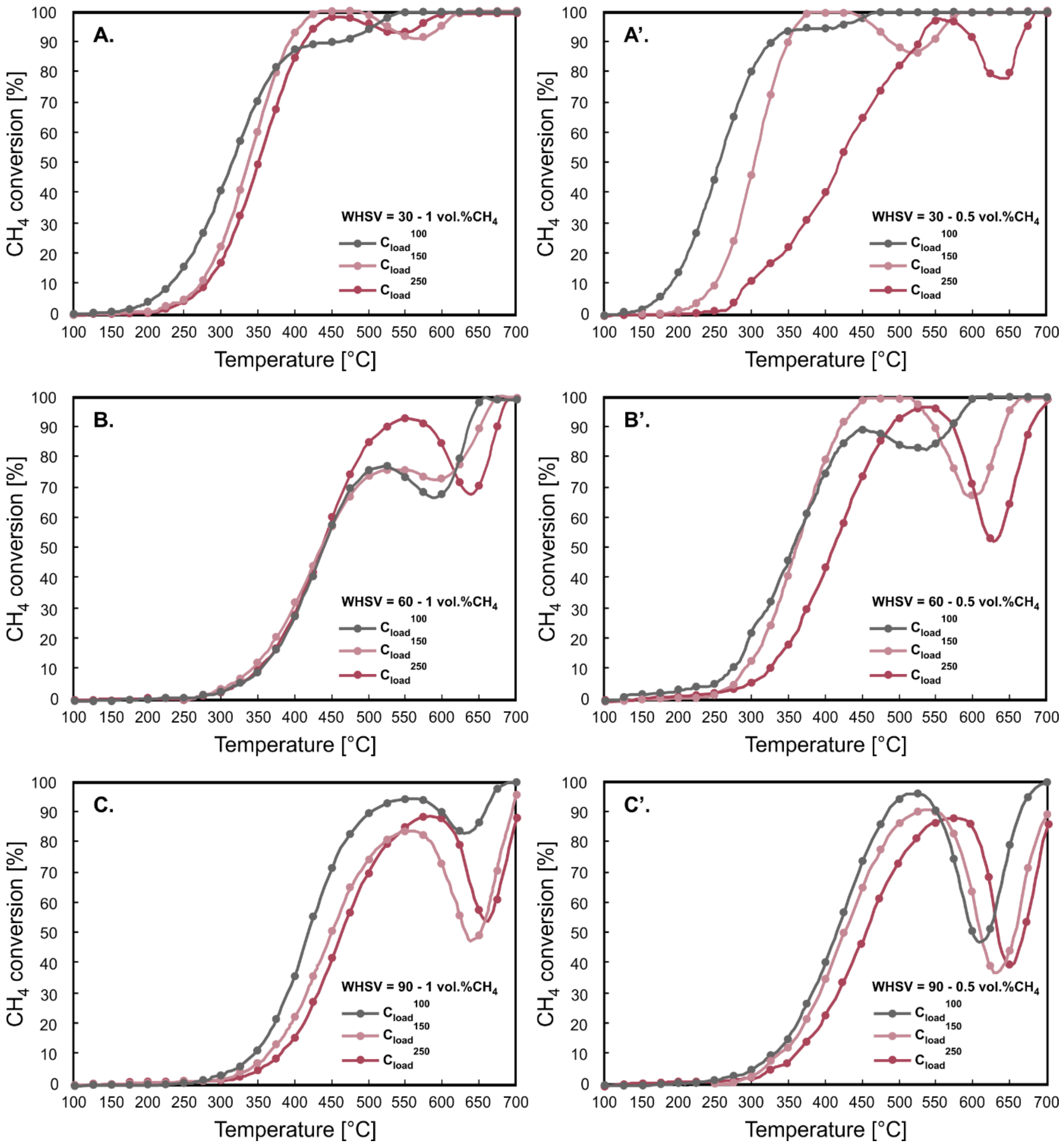

Figure 4. CH_4 conversion versus temperature by varying the Co_3O_4 load in the PdO/Co_3O_4 catalyst coated Zir-OCF at different WHSV and inlet CH_4 concentration.

Figure S3 in the *Supplementary Data* shows the characteristic temperatures T_{10}, T_{50}, and T_{90} corresponding to 10, 50, and 90% of CH_4 conversion (taken as the lowest temperature value obtained from light-off curves, **Fig.4**), by increasing WHSV for the three different catalyst loading. As general trend, for all WHSV and inlet CH_4 concentration, higher light-off temperatures (T_{10}) were obtained by increasing the Co_3O_4 amount. Similar trends were also obtained by comparing the temperatures at 50%

CH_4 conversion (T_{50}). On the other hand, it was more difficult to establish a specific trend for the T_{90} values when increasing the catalyst loading and the inlet CH_4 volume fraction because of the presence of the PdO-Pd transformation at high temperature. Interestingly, we recorded lower T_{10}, T_{50}, and T_{90} values at the highest WHSV (90 NL h^{-1} g_{cat}^{-1}) compared to those values obtained at 60 as WHSV, for the structured catalyst with the lowest amount of active phase, C_{load}^{100}, and when flowing the highest fraction of CH_4, 1 wt.%.

On the other hand, it is worth noting that for all catalytic tests, a decrease in CH_4 conversion is observed at medium/high temperatures. This drop in catalytic activity has been observed in numerous studies on methane oxidation over Pd-based catalysts, and was attributed to the decomposition of PdO to Pd and consequent Pd re-oxidation during the heating and cooling ramps, affecting negatively the catalytic reaction [38,41–47]. According to the literature, both transformations (PdO ↔ Pd decomposition and Pd ↔ PdO re-oxidation) occur via the formation of intermediate compounds identified as surface or interfacial PdO_x, which are the key species in the complete redox decomposition/re-oxidation reaction [38,44,48–51]. As mentioned above, all catalytic tests were carried out by cooling the reactor, that is, when the reactor reached the set temperature of 700 °C (by sending a flow of N_2), the reactive gas mixture was fed and once the steady-state conditions were achieved, the reactor was cooled down up to room temperature (cooling ramp of 5 °C min^{-1}). Hence, the decrease in CH_4 conversion obtained for all structured catalysts could be attributed to Pd re-oxidation. Colussi et al. [44] reported that the complete oxidation of the metal to the oxide that takes place during the cooling process is characterized as a kinetically-controlled process at high temperatures, which could explain the hysteresis observed. Further increase in catalytic activity by progressively decreasing the temperature is associated with the complete formation of the active phase (PdO), that is, the full oxidation of Pd. An additional interesting point is that by maintaining constant WHSV and catalyst loading (**Table S2**), when the reactor is fed with lower inlet CH_4 concentration, the hysteresis of the light-off curve is more accentuated (minor drop in CH_4 conversion). This could be explained by the fact that increasing the CH_4 inlet volume fraction in the reactor, maintaining the O_2/CH_4 molar ratio constant and equal to 8, leads to an increase of O_2 concentration and thus its partial pressure (ideal gas). Several authors suggest that increasing the partial pressure of O_2 helps to stabilize the PdO_x system by promoting the formation of PdO (active phase) as the temperature decreases (Pd ↔ PdO transformation) [43,44,46,48,49,52]. Farrauto et al. [41] also demonstrated using the thermogravimetric analysis that increasing oxygen concentration, both PdO decomposition and Pd re-oxidation shift to higher temperatures, where each temperature change corresponds to a different quasi-equilibrium oxygen content. In fact, as shown in **Table S2,** the ΔT of Pd-PdO transformation occurs at higher temperatures as the O_2 inlet concentration increased. Such an effect could also be due to the increased amount of PdO present on the foams when the overall catalyst load is increased.

Thus, taking into account the results obtained in this work and literature, we can infer that by increasing the Co_3O_4 load, the amount of oxygen present in the catalyst increases and hence a greater percentage of oxygen can be supplied during the Pd-PdO transformation, helping to stabilize the PdO_x species and shifting the Pd-PdO hysteresis to higher temperatures. Nevertheless, the strong interactions between metal and support could lead to a synergetic effect which is the key in the Co_3O_4 lattice oxygen supply for methane combustion in fuel-lean condition. In fact, recently we proposed a reaction scheme of the lean combustion of CH_4 using a catalytic powder of 3 wt.% PdO/Co_3O_4, with a series of XRF and XPS measurements we noted that bulk and surface composition of the catalysts is different [53]. Specifically, the surface concentration of Pd is higher than the bulk one, pointing out a strong interaction between Pd as active phase and Co_3O_4 as support carrying on oxygen, able to synergistically donate oxygen through an effective energy transfer via lattice vibrations involving surface Pd and oxygen ions [49].

Another interesting point to highlight from **Fig. 4** is that as the catalyst loading increases (by maintaining constant flow conditions), the light-off curves tend to shift towards higher temperatures, which could denote internal diffusional limitations. Since gases must diffuse through the catalyst pores to reach the catalytically active sites, an increase in catalyst loading leads to a thicker catalyst thickness, offering greater resistance to internal diffusion. Thus, a thicker catalyst thickness results in concentration gradients of the reactive species inside the catalyst, worsening the overall performance of the catalyst [54–56].

In the following section, we will evaluate the effect of Co_3O_4 amount on internal and external mass transfer.

2.3 Kinetic and mass transfer resistances analysis

To analyze the mass transfer effects that occur during the combustion reaction on the coated Zir-OCFs, we first determine the observed rate constant (k^{obs}), with the assumption of a pseudo-first order reaction because of the large excess of oxygen, according to the following equation:

$$k^{obs}(T) = \frac{1}{\tau} \cdot \ln\left(\frac{1}{1 - X_{CH4}(T)}\right) \quad (1)$$

$$\tau = \frac{W_{cat} \cdot C_{CH4}^{in}}{F_{CH4}^{in}} \quad (2)$$

where τ is the contact time (g_{cat} s m^{-3}), X_{CH4} is the conversion of methane, W_{cat} is the weight of 3 wt.% PdO/Co_3O_4 catalyst (g_{cat}) and C_{CH4}^{in}, F_{CH4}^{in} are the inlet concentration (mol m^{-3}) and molar flow of methane (mol s^{-1}), respectively. The logarithm of k^{obs} was plotted as a function of the inverse of the temperature according to the Arrhenius law.

Figure 5 shows a comparison of Arrhenius plots obtained at different catalyst contents for WHSV of 30 and inlet CH_4 concentration of 1 wt.%. By observing **Figure 5**, we can distinguish three characteristic zones for all catalyst loadings: I. at low temperatures (with $X_{CH4} < 5$ %), the reaction rate is very slow and the process is governed by the kinetic regime $\left(E_a \approx E_{app}\right)$; II. as the temperature increases, the internal diffusion limitations begin to appear reaching the point where the time for internal diffusion exceeds the reaction and external mass transfer time, thus, E_a drops at almost half of the slope obtained in the kinetic regime $\left(E_a \approx \frac{E_{app}}{2}\right)$ and the process is governed by the internal diffusion; and III., at sufficiently high temperatures, the performance of the catalyst depends solely on the external mass transfer from the bulk gas phase to the gas-catalyst interface, thus, the external diffusion takes control of the process ($E_a \approx 0$). The slopes in Figure 5, given by $\left(-\frac{E_a}{R}\right)$, are practically parallel, indicatinh similar apparent activatin energy values. The displacement of the C_{load}^{100} slope is due to the experimental points of the curve at low conversions. **Table S3** in the *Supplementary Data* lists the values of E_{app} with the related standard deviations. Analoguous plats can be obtained also for the other Co_3O_4 loads and WHSV (**Fig. S4** in the *Supplementary Data*).

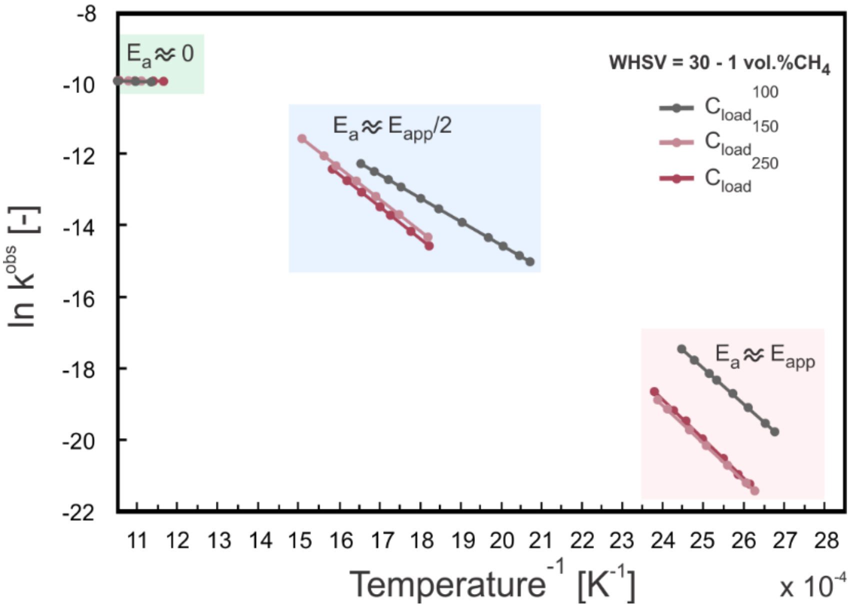

Figure 5. Arrhenius plots for tha various catalyst contents (C_{load}^{100}, C_{load}^{150}, and C_{load}^{250}) at WHSV of 30 and inlet CH$_4$ concentration of 1 wt.%.

Then, for the study of each controlling resistance during the lean oxidation of CH$_4$, we used the criteria developed in the grouo of Balakotaiah [57–60] for first order catalytic reactions in washcoated monolith, adapting the model to the OCF geometry. Consequently, it is possible to characterize the operation regimes by increasing the catalyst content on the foam. First of all, the characteristic length scales for transverse diffusion associated within gas phase ($R_{\Omega,e}$) and catalyst layer ($R_{\Omega,i}$) can be defined assuming circular shape of the foam pore and catalyst layer, that is, the catalyst is deposited uniformly within the internal wall of the pore forming a circular ring of thickness δ_c, as reported in our previous work [25] (**Fig. 6A and 6B**).

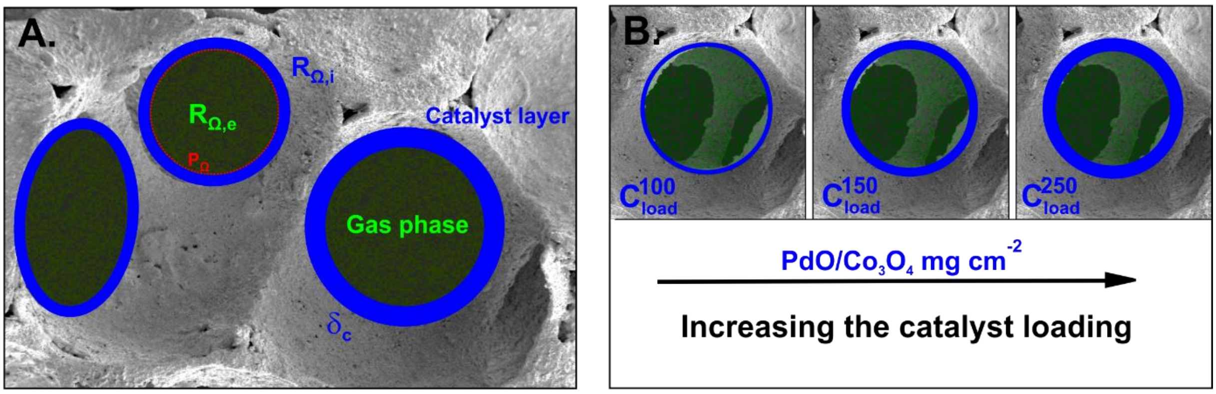

Figure 6. Characteristic length scales for transverse diffusion connected with gas phase and catalyst layer **(A)** and distribution of the PdO/Co_3O_4 catalytic layer on the pores' walls of the Zir-OCF with a circular shape by varying the Co_3O_4 amount **(B).**

For the gas phase, the characteristic length scale is defined as the ratio of the flow area ($A_{\Omega,e} = \frac{\pi \cdot {d_p^c}^2}{4}$) to the gas-catalyst layer interface perimeter ($P_\Omega = \pi \cdot d_p^c$), while for the the catalyst layer is defined as the ratio of the catalyst layer cross sectional area ($A_{\Omega,i} = \frac{\pi \cdot ({d_p^b}^2 - {d_p^c}^2)}{4}$) to the interfacial perimeter (P_Ω). It is important to note that $R_{\Omega,e}$ is related to the hydraulic diameter (d_h^c) by the expression $d_h^c = 4 \cdot R_{\Omega,e}$ and $R_{\Omega,i}$ corresponds to the effective catalyst thickness (δ_c).

$$R_{\Omega,e} = \frac{A_{\Omega,e}}{P_\Omega} = \frac{d_p^c}{4} = 4 \cdot d_h^c \tag{3}$$

$$R_{\Omega,i} = \frac{A_{\Omega,i}}{P_\Omega} = \frac{{d_p^b}^2 - {d_p^c}^2}{4 \cdot d_p^c} = \delta_c \tag{4}$$

where d_p^b and d_p^c are the diameter of the bare and catalyst coated OCF pore, respectively.

Next, we determined the external mass transfer coefficient (k_m^e) between the bulk of gas phase and the gas-catalyst layer interface as [58,59]:

$$k_m^e = \frac{Sh_e \cdot D_{CH4,mix}}{4 \cdot R_{\Omega,e}} = \frac{Sh_e \cdot D_{CH4,mix}}{d_h^c} \tag{5}$$

and the internal mass transfer coefficient (k_m^i) between the gas-catalytic layer interface and bulk of catalytic layer as [58,59]:

$$k_m^i = \frac{Sh_i \cdot D_{CH4,e}}{R_{\Omega,i}} = \frac{Sh_i \cdot D_{CH4,e}}{\delta_c} \tag{6}$$

where Sh_e, Sh_i are the external and internal Sherwood number, $D_{CH4,mix}$ and $D_{CH4,e}$ are the molecular and effective diffusivity of the CH_4 in the gas phase and within the catalyst layer, respectively.

To determine the Sh_e, we used the equation proposed by Balakotaiah and West [61] used for any arbitrary geometry:

$$Sh_e = Sh_{e,\infty} + 2.8 \cdot Sc^{\frac{1}{6}} \cdot P^{\frac{1}{2}} \tag{7}$$

To estimate Sh_i, we used the correlation proposed by Joshi et al. [58] for a first order reaction:

$$Sh_i = Sh_{i,\infty} + \frac{\Lambda \cdot \phi^2}{1 + \Lambda \cdot \phi} \tag{8}$$

where $Sh_{e,\infty}, Sh_{i,\infty}$ are the asymptotic external ($Sh_{e,\infty} = 3.656$) and internal ($Sh_{i,\infty} = 3.013$ [58]) Sherwood numbers for circular pore diameter and coated layer shape, Sc is the Schmidt number, P is the transverse Peclet number ($P = \frac{R_{\Omega,e}{}^2 \cdot u}{\tau_f \cdot L_f \cdot D_{CH4,mix}}$), Λ is a constant that depends on the catalyst layer geometry for first order reactions ($\Lambda = 0.38$ for a circular coated layer shape with circular crown ratio of 1.01 [58]) and ϕ is the Thiele modulus.

Hence, by considering the following assumptions: i. laminar and fully developed flow, ii. d_h^c much smaller than the OCF length (L_f), iii. isothermal conditions, and iv. first order kinetic; we can evaluate the overall resistance of the process in a coated OCF as:

$$R_t = R_m^e + R_m^i + R_r \tag{9}$$

$$R_m^e = \frac{1}{k_{m,e}}\ ; \qquad R_m^i = \frac{1}{k_{m,i}}\ ; \qquad R_r = \frac{1}{k \cdot R_{\Omega,i}} \tag{10}$$

where R_m^e, R_m^i are the resistances for external and internal mass transfer, R_r is the reaction resistance, R_t is the overall resistance of the process and k is the apparent first order reaction rate constant (s^{-1}). The latter calculated with the equation of Arrhenius considering only the experimental values with a CH_4 conversion lower than 5%.

Figure 7 shows a comparison of the evolution of the different regimes by varying the catalyst content on the foam at WHSV of 30 and 90 with inlet CH_4 concentration of 1 vol.%. As observed, all resistances show a decreasing trend with increasing temperature, although the diffusion resistances (R_m^e, R_m^i) are much less temperature sensitive compared to the reaction resistance (R_r), which is strongly dependent on the Arrhenius equation. As expected, at low temperatures, the reaction rate is much slower than the internal and external diffusion rate, thus, the reaction resistance is the controlling resistance ($R_r \gg R_m^e, R_m^i$). Particularly, C_{load}^{150} showed a wider temperature range under kinetic control at both WHSV (at $T < 300$ °C for WHSV = 30 and at $T < 388$ °C for WHSV = 90). As the temperature raises, the reaction rate raises and the diffusion effects begin to be significant in the process. The increase of the catalyst loading from 6.1 to 13.7 $mg_{cat}\ cm^{-2}{}_{OCF}$ led to a greater dominance of the R_m^i to lower temperatures at both gas velocities studied. These results are consistent with the light-off curves (**Fig**

4.), where as mentioned above, the increase of the catalyst loading shifted the CH_4 conversion curves to higher temperatures. To evaluate whether the combustion reaction was limited by internal diffusion, we used the Weisz-Prater criterion according to the following expression:

$$WP = \frac{r_{CH_4}^{obs} \cdot \delta_c^2}{D_{CH_4,e} \cdot C_{CH_4}^s} < 1 \tag{11}$$

where $r_{CH_4}^{obs}$ is the observed volumetric reaction rate for CH_4 (mol m^{-3} s^{-1}) and $C_{CH_4}^s$ is the CH_4 concentration at surface catalyst (mol m^{-3}).

It can be clearly noted from **Fig. S5**, the complete absence of internal diffusional limitations for C_{load}^{100} (corresponding to 6.1 mg_{cat} $cm^{-2}{}_{OCF}$). However, when increasing the catalyst loading to 8.2 and 13.7 mg_{cat} $cm^{-2}{}_{OCF}$, the WP values exceed unity, indicating diffusional limitations. For C_{load}^{150}, the WP number is higher than 1 at temperatures between 500-550 °C, then the value decays as a consequence of the conversion drop during Pd-PdO transformation and subsequently exceeds unity at 700 °C at WHSV of 90. For C_{load}^{250}, the WP number exceeds 1 at temperatures above 400° and 450°C at WHSV of 30 and 90, respectively. With regard to **Figure 4.B**, the fact that the curves are overlapping does not mean that diffusional problems are not present, but a consequence of the experimental data selected and their repeatability. From the WP criterion, it is evident that also for these data diffusional problems exist when the loading of catalyst is increased.

On the other hand at sufficiently high temperature, the R_m^e becomes dominant at lower WHSV (30) for the C_{load}^{100} and C_{load}^{250}. The analysis of the resistances and WP values at WHSV of 60 was characterized by intermediate values between those obtained at 30 and 90 WHSV (**Fig. S6** in the *Supplementary Data*). For a more detailed analysis, we plotted the ratio of each resistance to the total resistance as a function of temperature in **Figure 8**.

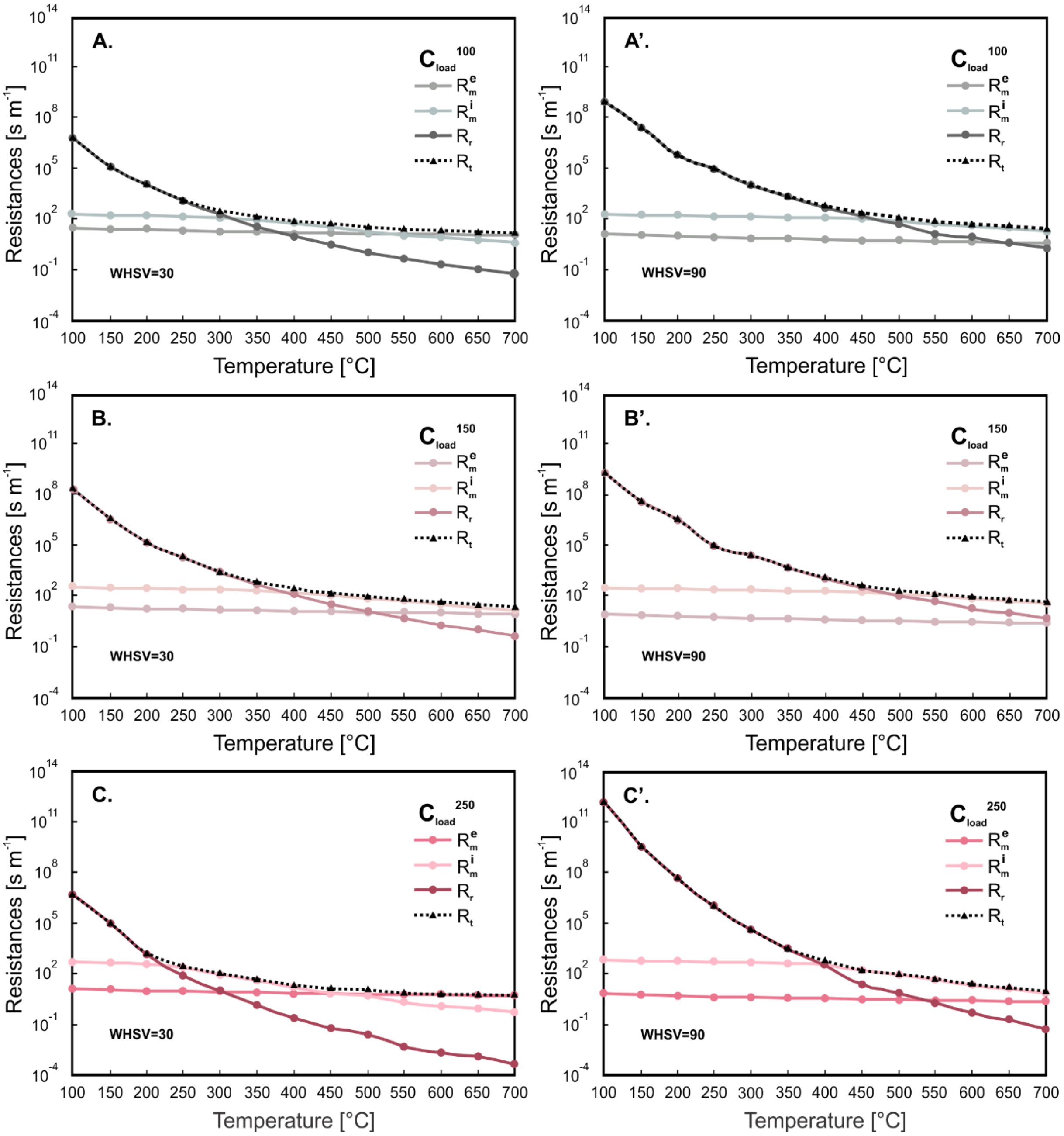

Figure 7. Various resistances versus temperature for the three catalyst contents at WHSV of 30 (**A,B** and **C**) and 90 (**A’**,**B’** and **C’**) for C_{load}^{100}, C_{load}^{150} and C_{load}^{250}, respectively.

For the C_{load}^{100}, the catalyst performance is controlled by the kinetic at temperatures below 240 and 365 °C at WHSV of 30 and 90 respectively, with an $\frac{R_r}{R_t} > 0.9$. At temperatures between 315 and 550 °C (at WHSV = 30) and above 470 °C (at WHSV = 90), the R_m^i is dominant with an $\frac{R_m^i}{R_t} > 0.5$ reaching a $\left[\frac{R_m^i}{R_t}\right]_{max}$ of 0.68 (at WHSV = 30) and 0.81 (at WHSV = 90) at 400 and 680 °C, respectively.

Interestingly, the slope for C_{load}^{100} at intermediate temperatures (where the internal mass transfer dominates) was lower than those obtained at higher catalyst loading (C_{load}^{150} and C_{load}^{250}), indicating a transitional regime between kinetic and external mass transfer control at WHSV of 30. At temperatures above 550 °C and WHSV of 30, the R_m^e dominates the performance ($\frac{R_m^e}{R_t} > 0.5$), achieving the $\left[\frac{R_m^e}{R_t}\right]_{max}$ of 0.81 at 700 °C. On the other hand, the raise of the gas velocity leads to a remarkable improvement of the external mass transfer where the $\left[\frac{R_m^e}{R_t}\right]_{max}$ reached at WHSV = 90 was of 0.12 at 700 °C.

By increasing the catalyst amount to C_{load}^{150}, the combustion is kinetically controlled at temperatures below 300 and 370 °C at WHSV of 30 and 90, respectively. At temperatures above 370 °C (WHSV = 30) and 473°C (WHSV = 90), R_m^i becomes the dominant resistance ($\frac{R_m^i}{R_t} > 0.5$) reaching the maximum ratio of 0.76 and 0.85 at 550 and 700 °C, respectively. The $\frac{R_m^e}{R_t}$ remained below 0.35 and 0.05 (at $T <$ 700 °C) for WHSV of 30 and 90, respectively.

Finally, at the highest catalyst loading (C_{load}^{250}), the complete kinetic regime $\frac{R_r}{R_t} > 0.9$ is found at temperatures below 170 °C (at WHSV = 30) and 338 °C (at WHSV = 90). At temperatures between 225 and 463 °C and WHSV of 30, the internal diffusion prevails ($\frac{R_m^i}{R_t} > 0.5$), where it reaches a maximum value of 0.85 at 300 °C. Above 463 °C, the R_m^e dominates the process, reaching the control at 700 °C ($\frac{R_m^e}{R_t} > 0.9$). On the other hand, at WHSV of 90, the combustion is dominated by the internal diffusion at temperatures above 400 °C, reaching a slight stability between 450 and 600 °C with $\frac{R_m^i}{R_t}$ values between 0.87 and 0.92. Thereafter, it starts to decrease reaching the value of 0.73 at 700 °C.

On the basis of the results obtained, we can generalize the discussion by considering the case of a catalyst supported on an open-cell foam, in which the temperature is systematically increased to span all the regimes of the catalytic process. Below, we describe in detail each of the regimes.

At low temperatures the reaction rate is much slower than the diffusion rates.The reaction occurs through the catalytic layer and the reactant concentration profile is nearly uniform. At this point, the reaction is controlled by kinetics that includes the processes of (i) adsorption of reactants on the active sites, (ii) catalytic reaction at the surface and (iii) desorption of products from the active sites. In this regime, the Thiele modulus, ϕ, (which describes the relationship between the rate of reaction and diffusion in a porous catalyst) is much lower than unity, while the effectiveness factor, η, (which is defined as the ratio of the observed reaction rate to the hypothetical rate in the absence of mass transfer limitations) is near unity. Thus, using **Equation. 9**, we can write: $R_t \approx R_r$ since $R_r \gg (R_m^e + R_m^i)$.

As the temperature increases, the reaction rate increases and diffusional limitations become important. If the characteristic time for internal diffusion is much higher than the reaction and external mass transfer time, strong intraparticle diffusional limitations will exist, whereby a concentration gradient will be present within the catalytic layer. A further increase of the temperature leads to an exponential increase of the reaction rate such that the characteristic reaction time is approximately zero and a reactant concentration gradient is formed at the fluid-catalyst layer interface. Strong internal and external concentration gradients will prevail. Finally, at sufficiently high temperatures, the performance of the catalytic foam will depend on mass transport from the bulk gas to the interface. At this point, the Thiele modulus is much larger than one, while the effectiveness factor tends to zero.

It is important to point out that the passage from one regime to another is given by a transition regime during which the catalyst operates. In this regime, the characteristic reaction and diffusion times are comparable. Furthermore, it is noteworthy that for highly fast reactions, the reactants are completely consumed on the external catalyst surface, whereby only the external mass transfer can influence the effective transformation rate. In this case, the internal mass transfer resistance is not considered. It is clear that the presence of each regime will depend on the different design and operating parameters such as catalyst thickness, foam dimensions, catalyst loading, reaction activation energy, effective diffusivity, etc.

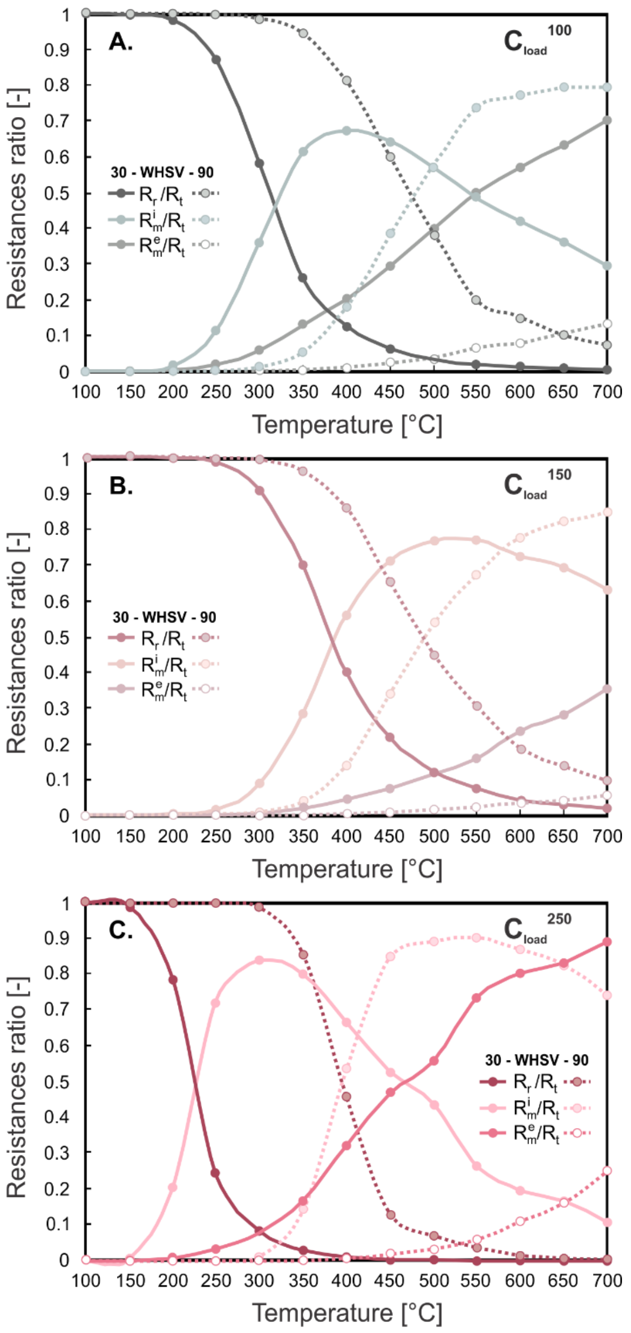

Figure 8. Ratio resistances as a function of temperature at WHSV of 30 and 90 for C_{load}^{100} (**A**), C_{load}^{150} (B) and C_{load}^{250} (C).

Thus, based on CH_4 conversion and mass transfer values obtained, the best performance for the full oxidation of methane in lean condition is provided by the structured catalyst with a loading of 6.1 mg_{cat} cm^{-2}_{OCF} (C_{load}^{100}), that is with the structured catalyst hosting the lower amount of active phase. These results are in agreement with those obtained in our previous works [11,62], where internal mass transfer limitations were observed at catalyst loads greater than 10 mg cm^{-2}, leading to a decrease in catalytic performance.

In the following section we will derive a correlation that describes the external mass transfer at low Reynolds number ($Re < 6$) for a catalyst-coated foam.

2.4 Mass transfer correlation for OCFs

Several correlations have been derived in the literature to investigate the external diffusion effects in OCFs as structured catalysts [4,5,15,17,19,21,63]. However, most of these correlations have been derived for Reynolds greater than 10, which make them inaccurate for the description of the process at low flow rates. For this purpose, we derived a correlation that allows to estimate the mass transfer coefficient at low Reynolds number, taking into consideration the parameters of the coated-OCF and considering a tetrakaidekahedral (TTKD) cell model, which has been well reported in many studies to be the configuration that best fits the OCF geometry [5,19,21]. For the flow conditions investigated (WHSV = 30, 60, 90;vol.$\%_{CH4}$= 0.5-1; P =1 atm), the external diffusion control was confirmed by the constancy of the conversion at elevated temperatures (temperatures higher than the temperature range where the Pd-PdO transformation occurs) with $\frac{R_m^e}{R_t} > 0.9$. Under full diffusive regime, the observed reaction rate is equal to the rate of transport of the reactants through the gas phase in steady-state conditions. Thus, the mass transfer coefficients can be estimated according to the steady-state CH_4 mass balance, considering isothermal plug flow reactor and negligible axial dispersion ($Pe > 50$) as:

$$k_{m,OCF}^{e} = -\frac{\ln(1-X_{CH4})}{Sv_{TTKD}\cdot(\frac{V_f}{F^v})} \tag{12}$$

where X_{CH4} is the methane conversion, Sv_{TTKD} is the specific surface area calculated assuming TTKD unit cell (m^2 m^{-3}), V_f is the foam volume (m^3) and F^v is the total volumetric flow of the gas mixture (m^3 s^{-1}).

Figure 9 shows the mass transfer coefficients by varying the amount of Co_3O_4 (with 3 wt.% of PdO) on the OCF with inlet CH_4 concentration of 1 vol.% as a function of WHSV. As observed, both the increase of the catalyst thickness on the foam and flow rate lead to an increase of the mass transfer coefficient.

As already stated, we considered the properties of the coated OCF and assumed that the catalyst was deposited uniformly on the inner wall of the foam pore with circular shape of the catalytic layer (**Fig. 6**), thus the thickness of the PdO/Co_3O_4 increases and the pore diameter available for the passage of the gas flow decreases. Therefore, as the pore diameter decreases, the higher the mass transfer coefficient. These results are consistent with those obtained in the literature [4,5,17,64]. For instance, Younis and Viskanta [64] used a single-blow transient technique to determine the volumetric heat transfer coefficient between the ceramic foam and a stream of air. That coefficient was strongly dependent on the average pore diameter, where the volumetric heat transfer coefficient increased with decreasing pore size. Giani and co-workers [4,17] also obtained an increase of the mass transfer coefficient with the decrease of the pore diameter in metallic foams. We attribute this effect to the fact that as the pore diameter decreases, the specific surface of the foam increases (S_v, m^2 m^{-3}), leading thus to a high fluid-to-solid mass transfer rate.

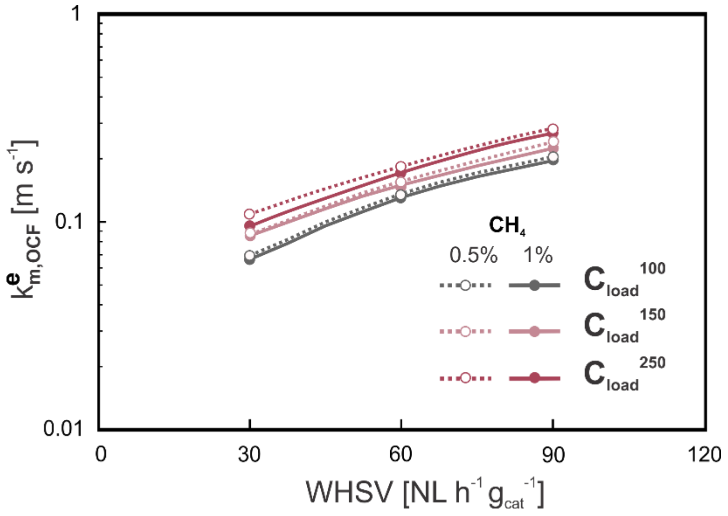

Figure 9. Mass-transfer coefficients versus inlet flow rate estimated for different catalyst loading at 1 and 0.5 vol.% of CH_4 concentration.

Mass transfer coefficients were expressed in dimensionless form ($Sh = \frac{k^e_{m,OCF} \cdot d^c_p}{D_{CH4,mix}}$), plotted against the Reynolds number on a logarithmic scale for all flow conditions investigated and fitted by a single correlation of the form $Sh = A \cdot Re^m \cdot Sc^{1/3}$ obtaining:

$$Sh = 1.07 \cdot Re^{0.55} \cdot Sc^{1/3} \tag{13}$$

where Re is the Reynolds number (considering as characteristic length the pore diameter of coated foam) and assuming Sherwood number dependency on the Schmidt number of $^1/_3$, as obtained from the boundary layer theory. This correlation was derived for the range of $0.75 < Re < 6$, foam void fraction of $0.75 < \varepsilon_o < 0.85$ and pore diameter of $1.24 < d_p < 1.38$ mm. **Figure 10** shows the derived correlation for the investigated OCFs (valid thus for zirconia, 30 ppi, covered different catalyst loadings).

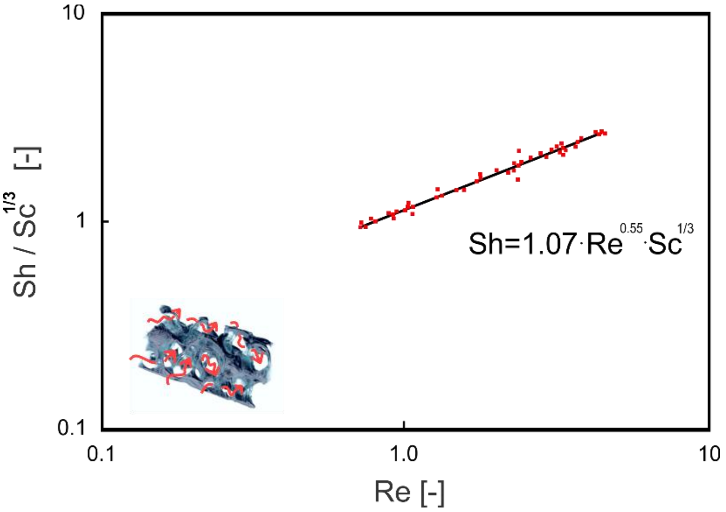

Figure 10. Mass-transfer coefficients versus inlet flow rate estimated for different catalyst loadings.

By comparing the correlation obtained with those derived from the literature [4,15–21], it is observed that the parameter A (which is a function of the porosity and geometric properties of the foam) is consistent with the values reported in various studies of foams of different material, both ceramic and metallic, (Al_2O_3 and FeCrAlloy), and cell densities (10-45 ppi) [4,5,17]. However, the exponent m that characterizes the dependence of Sherwood number with the magnitude of the velocity is slightly higher than the reported ones at relative high Re ($Re > 10$). Wen and Yu [65] investigated the mass transfer of naphthalene sublimation in a fixed bed where it was then fed into a converter and burned completely to CO_2 and H_2O. The data showed a nearly linear dependence ($m = 0.95$) of the Sherwood number with Reynolds at low flow velocities ($0.1 < Re < 5$). Later, Cybulski et al. [66] investigated the mass transport at low Reynolds numbers in a bed packed with silicon copper particles and air as a gaseous medium.

They confirmed the results obtained by Wen, obtaining a linear correlation for Reynolds range of (0.24 < Re < 0.63). Recently, Xu et al. [67] studied theoretically the mass transport from bulk fluid to pore surface in chemically reactive flows for ordered and disordered porous structures. The authors found that for disordered porous structures, the Sh increases linearly with Re at the creeping flow regime, while for Re > 10 a one-half power law dependence was exhibited. In a recently published study, Aguirre et al. [21] reported a correlation that describes the mass transfer in aluminum OCF coated with layers of Pt(1%)/γ-Al_2O_3 of thickness from 15 to 50 μm for the CO oxidation at low gas velocities (2 < Re < 20). They fitted the model to a correlation of the type: $Sh = Sh_\infty + A \cdot Re^m \cdot Sc^{1/3}$, where the Reynolds number dependency (m) was of 0.53, quite similar to the one obtained in this study. All these correlations, including the one reported in **Equation 13**, show a strong dependence on the Reynolds number (at low Re numbers), indicating a significant improvement in mass transfer by increasing the flow rate. It is also important to note that the correlation derived in this work, as well as those derived from the literature on both metallic and ceramic OCFs, show a weak dependence on flow velocity compared to unconsolidated systems where the solid phase is a discrete medium [21].

As next steps, we will expand our correlation to other porosities, and type of ceramic foams (alumina, cordierite or others).

5. Conclusions

This work studied the impact of catalyst loading by varying the Co_3O_4 amount (3 wt.% PdO on 100/150/250 mg Co_3O_4 spinel) coated on zirconia open cell foams (Zir-OCF) of 30 ppi used for the lean combustion of CH_4. The Co_3O_4 spinel was coated on the foams by solution combustion synthesis, while the PdO on the Co_3O_4 spinel by wetness impregnation. CH_4 combustion in lean conditions (0.5/1.0 vol.% CH_4 inlet combustion, 8 as O_2/CH_4 molar ratio, and 30, 60, and 90 as WHSV) was the investigated reaction model. According to the results obtained in this work, the main conclusions were the following:

- At the highest WHSV (90 NL h^{-1} g_{cat}^{-1}), only the catalyst loading of 6.1 mg_{cat} cm^{-2}_{OCF} (C_{load}^{100}) reached full conversion of CH_4 at temperatures below 700 °C for both the inlet CH_4 concentrations studied.

- As general trend, for all WHSV and inlet CH_4 concentration investigated, the increase of the Co_3O_4 amount led to an increase of the characteristic temperatures T_{10}, T_{50}, and T_{90}.
- The decrease in CH_4 conversion obtained for all structured catalysts could be attributed to Pd re-oxidation.
- The increase of the amount of Co_3O_4 led to a shifting of the light-off curve toward higher temperatures maintaining the Pd–PdO hysteresis and exhibiting a greater drop in CH_4 conversion.
- The increase of the catalyst loading from 6.1 to 13.7 $\mathrm{mg_{cat}\ cm^{-2}{}_{OCF}}$ led to a greater dominance of the internal mass transfer resistance (R_m^i) to lower temperatures at both gas velocities studied.
- The best performance for the complete CH_4 oxidation in lean condition was obtained with the catalyst loading of 6.1 $\mathrm{mg_{cat}\ cm^{-2}{}_{OCF}}$ (C_{load}^{100}).
- The mass transfer correlation derived in this study was found comparable with those derived from the literature, exhibiting a dependence of the Sherwood number with the Reynolds number slightly higher for $Re < 6$.

CRediT authorship contribution statement

Carmen W. Moncada Quintero: Conceptualization, Methodology, Investigation, Data curation, Formal analysis, Validation, Writing-Original draft preparation, Writing-Reviewing and Editing. **Giuliana Ercolino**: Conceptualization, Investigation, Data curation. **Stefania Specchia**: Conceptualization, Methodology, Validation. Supervision, Writing-Reviewing and Editing, Funding acquisition, Resources.

Declaration of competing interests

The authors declare that they have no known competing financial interests or personal relationships that could have appeared to influence the work reported in this paper.

Acknowledgements

This work was supported by the Italian Ministry of Education, University and Research (MIUR), via the ERANETMED EU-FP7 network (SOL-CARE project, grant number ENERG-065). The invaluable contribution to the electron microscopy observations of Mr Mauro Raimondo from the Politecnico di Torino is highly appreciated. The authors deeply acknowledge Prof. Radenka Maric, Vice President for Research of the University of Connecticut, for sponsoring the X-CT analyses, performed at the UCONN/Thermo Fisher Scientific Center for Advanced Microscopy and Materials Analysis (CAMMA).

References

[1] F. García-Moreno, Commercial applications of metal foams: Their properties and production, Materials (Basel). 9 (2016) 20–24. doi:10.3390/ma9020085.

[2] V. Papetti, P. Dimopoulos Eggenschwiler, A. Della Torre, F. Lucci, A. Ortona, G. Montenegro, Additive Manufactured open cell polyhedral structures as substrates for automotive catalysts, Int. J. Heat Mass Transf. 126 (2018) 1035–1047. doi:10.1016/j.ijheatmasstransfer.2018.06.061.

[3] I. Švecová, E. Tillová, L. Kuchariková, Improving the quality of Al-Si castings by using ceramic filters, Prod. Eng. Arch. 26 (2020) 19–24. doi:10.30657/pea.2020.26.05.

[4] L. Giani, G. Groppi, E. Tronconi, Mass-transfer characterization of metallic foams as supports for structured catalysts, Ind. Eng. Chem. Res. 44 (2005) 4993–5002. doi:10.1021/ie0490886.

[5] G. Incera Garrido, F.C. Patcas, S. Lang, B. Kraushaar-Czarnetzki, Mass transfer and pressure drop in ceramic foams: A description for different pore sizes and porosities, Chem. Eng. Sci. 63 (2008) 5202–5217. doi:10.1016/j.ces.2008.06.015.

[6] M. Bracconi, M. Ambrosetti, O. Okafor, V. Sans, X. Zhang, X. Ou, C.P. Da Fonte, X. Fan, M. Maestri, G. Groppi, E. Tronconi, Investigation of pressure drop in 3D replicated open-cell foams: Coupling CFD with experimental data on additively manufactured foams, Chem. Eng. J. 377 (2018) 120–123. doi:10.1016/j.cej.2018.10.060.

[7] G. Ercolino, P. Stelmachowski, S. Specchia, Catalytic Performance of Pd/Co_3O_4 on SiC and

ZrO_2 Open Cell Foams for Process Intensification of Methane Combustion in Lean Conditions, Ind. Eng. Chem. Res. 56 (2017) 6625–6636. doi:10.1021/acs.iecr.7b01087.

[8] E. Reichelt, M. Jahn, Generalized correlations for mass transfer and pressure drop in fiber-based catalyst supports, Chem. Eng. J. 325 (2017) 655–664. doi:10.1016/j.cej.2017.05.119.

[9] F.C. Buciuman, B. Kraushaar-Czarnetzki, Ceramic Foam Monoliths as Catalyst Carriers. 1. Adjustment and Description of the Morphology, Ind. Eng. Chem. Res. 42 (2003) 1863–1869. doi:10.1021/ie0204134.

[10] E. Tronconi, G. Groppi, C.G. Visconti, Structured catalysts for non-adiabatic applications, Curr. Opin. Chem. Eng. 5 (2014) 55–67. doi:10.1016/j.coche.2014.04.003.

[11] M.A. Ashraf, O. Sanz, C. Italiano, A. Vita, M. Montes, S. Specchia, Analysis of Ru/La-Al_2O_3 catalyst loading on alumina monoliths and controlling regimes in methane steam reforming, Chem. Eng. J. 334 (2018) 1792–1807. doi:10.1016/j.cej.2017.11.154.

[12] C. Italiano, M.A. Ashraf, L. Pino, C.W. Moncada Quintero, S. Specchia, A. Vita, Rh/CeO_2 thin catalytic layer deposition on alumina foams: Catalytic performance and controlling regimes in biogas reforming processes, Catalysts. 8 (2018) 1–25. doi:10.3390/catal8100448.

[13] S. Voltolina, P. Marín, F.V. Díez, S. Ordóñez, Open-cell foams as beds in multiphase reactors: Residence time distribution and mass transfer, Chem. Eng. J. 316 (2017) 323–331. doi:10.1016/j.cej.2017.01.113.

[14] A. Klegova, A. Inayat, P. Indyka, J. Gryboś, Z. Sojka, K. Pacultová, W. Schwieger, A. Volodarskaja, P. Kuśtrowski, A. Rokicińska, D. Fridrichová, L. Obalová, Cobalt mixed oxides deposited on the SiC open-cell foams for nitrous oxide decomposition, Appl. Catal. B Environ. 255 (2019). doi:10.1016/j.apcatb.2019.117745.

[15] J.T. Richardson, D. Remue, J.K. Hung, Properties of ceramic foam catalyst supports: Mass and heat transfer, Appl. Catal. A Gen. 250 (2003) 319–329. doi:10.1016/S0926-860X(03)00287-4.

[16] F.C. Patcas, G.I. Garrido, B. Kraushaar-Czarnetzk, CO oxidation over structured carriers: a comparison of ceramic foams, honeycombs and beads, Chem. Eng. Sci. 62 (2007) 3984–3990. doi:10.1016/j.ces.2007.04.039.

[17] G. Groppi, L. Giani, E. Tronconi, Generalized correlation for gas/solid mass-transfer

coefficients in metallic and ceramic foams, Ind. Eng. Chem. Res. 46 (2007) 3955–3958. doi:10.1021/ie061330g.

[18] F. Lucci, A. Della Torre, J. von Rickenbach, G. Montenegro, D. Poulikakos, P. Dimopoulos Eggenschwiler, Performance of randomized Kelvin cell structures as catalytic substrates: Mass-transfer based analysis, Chem. Eng. Sci. 112 (2014) 143–151. doi:10.1016/j.ces.2014.03.023.

[19] A. Della Torre, F. Lucci, G. Montenegro, A. Onorati, P. Dimopoulos Eggenschwiler, E. Tronconi, G. Groppi, CFD modeling of catalytic reactions in open-cell foam substrates, Comput. Chem. Eng. 92 (2016) 55–63. doi:10.1016/j.compchemeng.2016.04.031.

[20] S. De Schampheleire, P. De Jaeger, K. De Kerpel, B. Ameel, H. Huisseune, M. De Paepe, How to study thermal applications of open-cell metal foam: Experiments and computational fluid dynamics, Materials (Basel). 9 (2016) 1–27. doi:10.3390/ma9020094.

[21] A. Aguirre, V. Chandra, E.A.J.F. Peters, J.A.M. Kuipers, M.F. Neira D'Angelo, Open-cell foams as catalysts support: A systematic analysis of the mass transfer limitations, Chem. Eng. J. 393 (2020) 124656. doi:10.1016/j.cej.2020.124656.

[22] J. von Rickenbach, F. Lucci, C. Narayanan, P. Dimopoulos Eggenschwiler, D. Poulikakos, Effect of washcoat diffusion resistance in foam based catalytic reactors, Chem. Eng. J. 276 (2015) 388–397. doi:10.1016/j.cej.2015.03.132.

[23] G. Ercolino, G. Grzybek, P. Stelmachowski, S. Specchia, A. Kotarba, V. Specchia, Pd/Co_3O_4-based catalysts prepared by solution combustion synthesis for residual methane oxidation in lean conditions, Catal. Today. 257 (2015) 66–71. doi:10.1016/j.cattod.2015.03.006.

[24] G. Ercolino, S. Karimi, P. Stelmachowski, S. Specchia, Catalytic combustion of residual methane on alumina monoliths and open cell foams coated with Pd/Co_3O_4, Chem. Eng. J. 326 (2017) 339–349. doi:10.1016/j.cej.2017.05.149.

[25] C.W. Moncada, G. Ercolino, A. Poozhikunnath, Analysis of heat and mass transfer limitations for the combustion of methane emissions on PdO/Co_3O_4 coated on ceramic open cell foams, Chem. Eng. J. 405 (2021) 126970. doi:10.1016/j.cej.2020.126970.

[26] S. Specchia, C. Galletti, V. Specchia, Solution Combustion Synthesis as intriguing technique to quickly produce performing catalysts for specific applications, Elsevier Masson SAS, 2010.

doi:10.1016/S0167-2991(10)75008-4.

[27] S. Specchia, G. Ercolino, S. Karimi, C. Italiano, A. Vita, Solution combustion synthesis for preparation of structured catalysts: A mini-review on process intensification for energy applications and pollution control, Int. J. Self-Propagating High-Temperature Synth. 26 (2017) 166–186. doi:10.3103/S1061386217030062.

[28] J. Große, B. Dietrich, H. Martin, M. Kind, J. Vicente, E.H. Hardy, Volume image analysis of ceramic sponges, Chem. Eng. Technol. 31 (2008) 307–314. doi:10.1002/ceat.200700403.

[29] T.W. Ridler, S. Calvard, Picture Thresholding Using, IEEE Trans. Syst. Man Cybern. smc-8 (1978) 630–632.

[30] P.L. Smith, D.B. Reid, A Tlreshold Selection Method from Gray-Level Histograms, IEEE Trans. Syst. Man Cybern. 20 (1979) 62–66.

[31] S. Neethirajan, C. Karunakaran, D.S. Jayas, N.D.G. White, X-ray Computed Tomography Image Analysis to explain the Airflow Resistance Differences in Grain Bulks, Biosyst. Eng. 94 (2006) 545–555. doi:10.1016/j.biosystemseng.2006.04.013.

[32] T.B. Kim, S. Yue, Z. Zhang, E. Jones, J.R. Jones, P.D. Lee, Additive manufactured porous titanium structures: Through-process quantification of pore and strut networks, J. Mater. Process. Technol. 214 (2014) 2706–2715. doi:10.1016/j.jmatprotec.2014.05.006.

[33] A. Inayat, H. Freund, T. Zeiser, W. Schwieger, Determining the specific surface area of ceramic foams: The tetrakaidecahedra model revisited, Chem. Eng. Sci. 66 (2011) 1179–1188. doi:10.1016/j.ces.2010.12.031.

[34] M.A. Ashraf, O. Sanz, M. Montes, S. Specchia, Insights into the effect of catalyst loading on methane steam reforming and controlling regime for metallic catalytic monoliths, Int. J. Hydrogen Energy. 43 (2018) 11778–11792. doi:10.1016/j.ijhydene.2018.04.126.

[35] A.K. Datye, J. Bravo, T.R. Nelson, P. Atanasova, M. Lyubovsky, L. Pfefferle, Catalyst microstructure and methane oxidation reactivity during the Pd↔PdO transformation on alumina supports, Appl. Catal. A Gen. 198 (2000) 179–196. doi:10.1016/S0926-860X(99)00512-8.

[36] B.A. P.A. Carlsson, M. Skoglundh, E. Fridell, E. Jobson, Induced low temperature catalytic

ignition by transient changes in the gas composition, Catal. Today. 73 (2002) 307–313. doi:10.1016/j.cej.2010.10.051.

[37] S. Specchia, S. Tacchino, V. Specchia, Facing the catalytic combustion of CH_4/H_2 mixtures into monoliths, Chem. Eng. J. 167 (2011) 622–633. doi:0.1016/j.cej.2010.10.051.

[38] M. Cargnello, J.J. Delgado Jaén, J.C. Hernández Garrido, K. Bakhmutsky, T. Montini, J.J. Calvino Gámez, R.J. Gorte, P. Fornasiero, Exceptional activity for methane combustion over modular Pd@CeO_2 subunits on functionalized Al_2O_3, Science (80-.). 337 (2012) 713–717. doi:10.1126/science.1222887.

[39] A.T. S. Colussi, P. Fornasiero, Structure-activity relationship in Pd/CeO_2 methane oxidation catalysts, Chinese J. Catal. 41 (2020) 938–950. doi:10.1016/S1872-2067(19)63510-2.

[40] J. Lin, X. Chen, Y. Zheng, F. Huang, Y. Xiao, Y. Zheng, L. Jiang, Facile construction of ultrastable alumina anchored palladium catalysts: via a designed one pot strategy for enhanced methane oxidation, Catal. Sci. Technol. 10 (2020) 4612–4623. doi:10.1039/d0cy00727g.

[41] R.J. Farrauto, M.C. Hobson, T. Kennelly, E.M. Waterman, Catalytic chemistry of supported palladium for combustion of methane, Appl. Catal. A, Gen. 81 (1992) 227–237. doi:10.1016/0926-860X(92)80095-T.

[42] G. Groppi, C. Cristiani, L. Lietti, P. Forzatti, Study of PdO/Pd transformation over alumina supported catalysts for natural gas combustion, Stud. Surf. Sci. Catal. 130 D (2000) 3801–3806. doi:10.1016/s0167-2991(00)80615-1.

[43] L.M.T. Simplício, S.T. Brandão, D. Domingos, F. Bozon-Verduraz, E.A. Sales, Catalytic combustion of methane at high temperatures: Cerium effect on PdO/Al_2O_3 catalysts, Appl. Catal. A Gen. 360 (2009) 2–7. doi:10.1016/j.apcata.2009.03.005.

[44] S. Colussi, A. Trovarelli, E. Vesselli, A. Baraldi, G. Comelli, G. Groppi, J. Llorca, Structure and morphology of Pd/Al_2O_3 and Pd/CeO_2/Al_2O_3 combustion catalysts in Pd-PdO transformation hysteresis, Appl. Catal. A Gen. 390 (2010) 1–10. doi:10.1016/j.apcata.2010.09.033.

[45] M. Danielis, S. Colussi, C. De Leitenburg, L. Soler, J. Llorca, A. Trovarelli, The effect of milling parameters on the mechanochemical synthesis of Pd-CeO_2 methane oxidation catalysts,

Catal. Sci. Technol. 9 (2019) 4232–4238. doi:10.1039/c9cy01098j.

[46] S. Nasr, N. Semagina, R.E. Hayes, Kinetic Modelling of C_o3O_4- and Pd/Co_3O_4-Catalyzed Wet Lean Methane Combustion, Emiss. Control Sci. Technol. 6 (2020) 269–278. doi:10.1007/s40825-019-00143-0.

[47] J. Shen, R.E. Hayes, N. Semagina, On the contribution of oxygen from Co_3O_4 to the Pd-catalyzed methane combustion, Catal. Today. 360 (2019) 435–443. doi:10.1016/j.cattod.2019.12.041.

[48] D. Ciuparu, E. Altman, L. Pfefferle, Contributions of lattice oxygen in methane combustion over PdO-based catalysts, J. Catal. 203 (2001) 64–74. doi:10.1006/jcat.2001.3331.

[49] Y.H.C. Chin, M. García-Diéguez, E. Iglesia, Dynamics and thermodynamics of Pd-PdO phase transitions: Effects of pd cluster size and kinetic implications for catalytic methane combustion, J. Phys. Chem. C. 120 (2016) 1446–1460. doi:10.1021/acs.jpcc.5b06677.

[50] M. Monai, T. Montini, R.J. Gorte, P. Fornasiero, Catalytic Oxidation of Methane: Pd and Beyond, Eur. J. Inorg. Chem. 2018 (2018) 2884–2893. doi:10.1002/ejic.201800326.

[51] H. Stotz, L. Maier, A. Boubnov, A.T. Gremminger, J.D. Grunwaldt, O. Deutschmann, Surface reaction kinetics of methane oxidation over PdO, J. Catal. 370 (2019) 152–175. doi:10.1016/j.jcat.2018.12.007.

[52] R. Gholami, M. Alyani, K.J. Smith, Deactivation of Pd catalysts by water during low temperature methane oxidation relevant to natural gas vehicle converters, 2015. doi:10.3390/catal5020561.

[53] G. Ercolino, P. Stelmachowski, G. Grzybek, A. Kotarba, S. Specchia, Optimization of Pd catalysts supported on Co_3O_4 for low-temperature lean combustion of residual methane, Appl. Catal. B Environ. 206 (2017) 712–725. doi:10.1016/j.apcatb.2017.01.055.

[54] B. Millington, V. Whipple, B.G. Pollet, A novel method for preparing proton exchange membrane fuel cell electrodes by the ultrasonic-spray technique, J. Power Sources. 196 (2011) 8500–8508. doi:10.1016/j.jpowsour.2011.06.024.

[55] G. Arzamendi, P.M. Die, L.M. Gandı, Renewable hydrogen technologies: Renewable hydrogenenergy - An overview, 2013. doi:10.1016/B978-0-444-56352-1.00001-5.

[56] J.J. Spivey, K.M. Dooley, Catalysis, The Royal Society of Chemistry, 2009.

[57] M. Bhattacharya, M.P. Harold, V. Balakotaiah, Mass-transfer coefficients in washcoated monoliths, AIChE J. 50 (2004) 2939–2955. doi:10.1002/aic.10212.

[58] S.Y. Joshi, M.P. Harold, V. Balakotaiah, On the use of internal mass transfer coefficients in modeling of diffusion and reaction in catalytic monoliths, Chem. Eng. Sci. 64 (2009) 4976–4991. doi:10.1016/j.ces.2009.08.008.

[59] S.Y. Joshi, M.P. Harold, V. Balakotaiah, Overall mass transfer coefficients and controlling regimes in catalytic monoliths, Chem. Eng. Sci. 65 (2010) 1729–1747. doi:10.1016/j.ces.2009.11.021.

[60] S.Y. Joshi, Y. Ren, M.P. Harold, V. Balakotaiah, Determination of kinetics and controlling regimes for H2 oxidation on Pt/Al_2O_3 monolithic catalyst using high space velocity experiments, Appl. Catal. B Environ. 102 (2011) 484–495. doi:10.1016/j.apcatb.2010.12.030.

[61] V. Balakotaiah, D.H. West, Shape normalization and analysis of the mass transfer controlled regime in catalytic monoliths, Chem. Eng. Sci. 57 (2002) 1269–1286. doi:10.1016/S0009-2509(02)00059-3.

[62] S. Wójcik, G. Ercolino, M. Gajewska, C.W. Moncada Quintero, S. Specchia, A. Kotarba, Robust $Co_3O_4|\alpha\text{-}Al_2O_3|$cordierite structured catalyst for N_2O abatement – Validation of the SCS method for active phase synthesis and deposition, Chem. Eng. J. 377 (2018) 120088. doi:10.1016/j.cej.2018.10.025.

[63] M. Bracconi, M. Ambrosetti, M. Maestri, G. Groppi, E. Tronconi, A fundamental analysis of the influence of the geometrical properties on the effective thermal conductivity of open-cell foams, Chem. Eng. Process. - Process Intensif. 129 (2018) 181–189. doi:10.1016/j.cep.2018.04.018.

[64] L.B. Younis, R. Viskanta, Experimental determination of the volumetric heat transfer coefficient between stream of air and ceramic foam, Int. J. Heat Mass Transf. 36 (1993) 1425–1434. doi:10.1016/S0017-9310(05)80053-5.

[65] C.Y. Wen, Y.H. Yu, A generalized method for predicting the minimum fluidization velocity, AIChE J. 12 (1966) 610–612. doi:10.1002/aic.690120343.

[66] A. Cybulski, M.J. Van Dalen, J.W. Verkerk, P.J. Van Den Berg, Gas-particle heat transfer coefficients in packed beds at low Reynolds numbers, Chem. Eng. Sci. 30 (1975) 1015–1018. doi:10.1016/0009-2509(75)87002-3.

[67] A. Xu, T.S. Zhao, L. Shi, J.B. Xu, Lattice Boltzmann Simulation of Mass Transfer Coefficients for Chemically Reactive Flows in Porous Media, J. Heat Transfer. 140 (2018) 1–8. doi:10.1115/1.4038555.